AIMS *Mathematics*

Research article

An artificial neural network analysis of the thermal distribution of a fractional-order radial porous fin influenced by an inclined magnetic field

M. A. El-Shorbagy[1,2], **Waseem**[3,*], **Mati ur Rahman**[4,5,*], **Hossam A. Nabwey**[1,2] and **Shazia Habib**[6,7]

1 Department of Mathematics, College of Science and Humanities in Al-Kharj, Prince Sattam bin Abdulaziz University, Al-Kharj 11942, Saudi Arabia

2 Department of Basic Engineering Science, Faculty of Engineering, Menoufia University, Shebin El-Kom 32511, Egypt

3 School of Mechnical Engineering, Jiangsu University, Zhenjiang 212013, Jiangsu, China

4 School of Mathematical Sciences, Jiangsu University, Zhenjiang 212013, Jiangsu, China

5 Department of Computer Science and Mathematics, Lebanese American University, Beirut, Lebanon

6 Department of Mathematics, Abdul Wali Khan University Mardan, Khyber Pakhtunkhwa 23200, Pakistan

7 Department of Mathematics, University of Engineering and Technology Mardan, Khyber Pakhtunkhwa 23200, Pakistan

* **Correspondence:** Email: waseem@ujs.edu.cn; matimaths@ujs.edu.cn.

Abstract: Fins and radial fins are essential elements in engineering applications, serving as critical components to optimize heat transfer and improve thermal management in a wide range of sectors. The thermal distribution within a radial porous fin was investigated in this study under steady-state conditions, with an emphasis on the impact of different factors. The introduction of an inclined magnetic field was investigated to assess the effects of convection and internal heat generation on the thermal behavior of the fin. The dimensionless form of the governing temperature equation was utilized to facilitate analysis. Numerical solutions were obtained through the implementation of the Hybrid Cuckoo Search Algorithm-based Artificial Neural Network (HCS-ANN). The Hartmann number (M) and the Convection-Conduction parameter (Nc) were utilized in the evaluation of heat transfer efficiency. Enhanced efficiency, as evidenced by decreased temperature and enhanced heat removal, was correlated with higher values of these parameters. Residual errors for both M and Nc were contained within a specified range of 10^{-6} to 10^{-14}, thereby offering a quantitative assessment of the model's accuracy. As a crucial instrument for assessing the performance and dependability of predictive models, the residual analysis highlighted the impact of fractional orders on temperature

fluctuations. As the Hartmann number increased, the rate of heat transfer accelerated, demonstrating the magnetic field's inhibitory effect on convection heat transport, according to the study. The complex relationship among Nc, fractional order (BETA), and temperature was underscored, which motivated additional research to improve our comprehension of the intricate physical mechanisms involved. This study enhanced the overall understanding of thermal dynamics in radial porous fins, providing significant implications for a wide array of applications, including aerospace systems and heat exchangers.

1. Introduction

There has been a rise in recent years in the importance of enhancing thermal transmission capacities in high-tech production settings. Conventional methods of heat transmission, which rely on base liquids including water, ethylene glycol, oil, and petroleum, struggle to attain ideal heat exchange rates due to their low thermal conductivity. Researchers have been concentrating on improving heat conductivity using nanoliquids as a means of getting around this problem. When nanoparticles are dispersed in a base fluid, a nanofluid is created with superior thermophysical characteristics to hydrogels. Due to their superior thermal qualities, they have replaced traditional coolants in radiators, electronic coolers, and heat exchangers.

In an effort to comprehend the complexities of heat transfer, a multitude of scholars have investigated the behavior of nanoliquids as they traverse a variety of geometries, taking into account a multitude of consequential factors [1–4]. Furthermore, there has been an increase in the strategic implementation of extended surfaces, also referred to as fins, to enhance heat dissipation from a heated surface via convective, radiative, or convective–radiative mechanisms. The thermal behavior of fins is of the utmost importance in a wide range of applications, such as circuit board cooling, heat exchangers, heat-rejection mechanisms in spacecraft, and electronic component cooling systems. In addition to their traditional uses, fins have demonstrated their effectiveness in a wide range of contexts.

An exhaustive review of the relevant literature reveals that thermal analysis of various fin designs has been the subject of an abundance of research [5–8]. The aforementioned collection of research highlights the importance of fins in enhancing the efficiency of heat dissipation mechanisms, providing valuable perspectives on the complex interaction between nanofluids and fin configurations. The ongoing pursuit of improvements in heat transmission has generated significant interest in the potential of integrating nanofluids and novel fin designs to advance thermal management in a wide range of industrial and technological contexts. In numerous industrial contexts, fin designers strive to optimize thermal transfer while reducing fin size and cost, with a specific emphasis on refrigeration, air conditioning, and the chilling of technical devices. The regulation of thermal management systems by fins guarantees their long lifespan and optimal performance. The examination of heat transport

mechanisms in fins, with a specific focus on radially structured fins, is of paramount importance in the pursuit of technologically sophisticated and economically viable engineering solutions. The findings of these inquiries indicate promise for real-world applications in which efficient heat dissipation is a critical component, affecting the environmental sustainability and overall performance of diverse technical systems. Kim et al. [9] studied the impact of porous fins on heat transfer and pressure reduction in plate-fin heat exchangers, finding that permeability and porosity significantly affect friction and heat transfer rate. Fathi et al. [10] found porous-fin microchannels better than solid-fin microchannels when channel height is low. Sowmya et al. [11] studied the temperature distribution in a porous plate under convection, radiation, and internal heat generation conditions. Gireesha et al. [12] assessed thermal characteristics of inclined porous fins, while Wang et al. [13] found metallic foam heat sinks have enhanced cooling capabilities.

In recent times, there has been a marked emphasis in the field of thermal engineering on improving heat transmission within porous media, owing to their remarkable dense thermal conductivities. Utilizing porous media, which provide a considerable surface area for heat transfer, can substantially enhance the efficiency of heat exchange apparatus. The optimization of convective heat transfer, which finds utility in combustion chambers, catalysts, and electronic component cooling, has been the subject of extensive research. Further investigations are being conducted to determine the effects of porous media on fins, which may result in improved heat dissipation for a variety of applications. Kumar et al. [3] study on radial porous fin thermal distribution found optimal heat transfer through thermal convection and an inclined magnetic field. The study also revealed that variations in magnetic field angle increased heat transfer rate while decreasing temperature. The combined efforts of the researchers [14–16] make a substantial contribution to the overall comprehension of thermal dynamics and entropy factors in various configurations of permeable fins. The inquiries considered various influential factors, such as magnetic forces, radiation, convection, and internal heat generation, thereby enhancing comprehension of heat transfer phenomena occurring within porous structures. The influence of a magnetic field is pervasive throughout an array of technological domains, including but not limited to metal casting, molten metal purification, and nuclear reactor coolant. The strategic utilization of an external magnetic field becomes a potent instrument for controlling convective heat transfer rates within the domain of thermal engineering. As a result, extended scholarly interest has been devoted to the examination of the impact of magnetic fields, which has generated an abundance of publications detailing the profound consequences of magnetic forces on fin heat transmission [17–19]. This collection of research not only enhances our fundamental comprehension of heat transfer phenomena but also demonstrates the adaptability and influence of magnetic fields in advancing thermal engineering technologies in a variety of applications where controlled heat manipulation is of the utmost importance. Selimefendigil et al. [20] investigated the effects of a magnetic field and an elastic fin on the dynamics of phase change within a cylindrical reactor embedded with a PCM-packed bed. The efficacy of the magnetic field was observed across various fin diameters and vertical orientations. Kumar et al. [21] studied the effect of an internal heat source and an electromagnetic field on the thermal distribution over a longitudinal trapezoidal porous fin. The fractional arrangement Operating (ODEs) and (PDEs) play a vital role in the fields of fluid mechanics and engineering by offering precise depictions of intricate phenomena such as those occurring in porous media, shallow water dynamics, heat transfer enhancement, biomedical fluid dynamics, hydrodynamic stability analysis, optimization of fluid transport systems,

modeling of oil reservoirs, aerodynamics, and aircraft design. The methods used for the porous fin problems have been investigated by researchers by applying different techniques, such as multigrid method, multigrid-homotopy method, and wavelet multiscale method, have recently been applied to many practical application problems, such as [22–24]. The comprehension of all the above are facilitated by these equations. Their significance and adaptability in these domains attest to their substantial contribution to the progression of knowledge and capacities in the disciplines of fluid mechanics and engineering. Derivatives and integrals of fractional orders have undergone substantial advancements over the last ten years, as supported by an abundance of scholarly monographs and research papers devoted to the subject. A multitude of mathematical models that incorporate fractional calculus have been investigated across disciplines, including epidemiology, differential-difference equations, vibration equations, and heat transfer, among others [25–27]. In a recent publication [28–31], Caputo and Fabrizio presented a fractional derivative that holds significant utility in elucidating mechanical phenomena such as damage, wear, plasticity, and electromagnetic hysteresis. This novel derivative is especially well-suited for processes that do not need these effects. In order to comprehend groundwater flow, reaction-diffusion equations, and nonlinear models, scientists have implemented this derivative. Moreover, in various scientific domains, alternative fractional derivatives utilizing non-singular kernels have been suggested and implemented, demonstrating the adaptability and practicality of these mathematical principles [32, 33].

Within the domains of engineering and fluid mechanics, artificial neural networks (ANNs) function as essential instruments that find extensive utility. ANNs are utilized extensively in materials science, computational fluid dynamics (CFD), pattern recognition, predictive modeling, control systems, fault detection, optimization, fluid flow modeling, turbulence modeling, and heat transfer analysis. By extracting features from sensor data or images, these devices enable the classification of data points; they can also predict complex system behaviors, control parameters, identify abnormal behavior or defects, optimize engineering processes, and forecast material properties. Artificial neural networks (ANNs) are of great significance in tackling intricate problems in various engineering fields [34–36]. They provide a resilient and adaptable methodology for examining, representing, and enhancing complex systems and procedures. Scholars [37–39] have investigated non-Fourier irregular heat transfer in a trapezoidal porous fin, transient thermal dispersion in a moving plate, and the influence of radiation on nanofluid mixed convection in a circular cylinder by employing the Levenberg-Marquardt backpropagation artificial neural network technique. The results of this study underscore the efficacy of incorporating artificial neural networks into diverse heat transfer models. The material properties of rectangular porous fins were analyzed by Waseem et al. [40] using a neural computer model and a metaheuristic technique. They used the Cuckoo search method to find the optimal temperature profile for the process. They also analyzed a convective straight fin with fractional order and thermal conductivity variables.

As for the novelty of this manuscript, by acknowledging the critical nature of heat transfer and the difficulties that accompany it, we present an innovative fractional model for the energy balance equation that integrates the recently developed Caputo-Fabrizio fractional derivative. The purpose of this model is to assess the performance of convective radial fins, which possess the thermal conductivity that varies with temperature. In order to tackle the complexities presented by the fractional order energy balance equation, we employ a novel methodology that integrates the state-of-the-art Cuckoo search algorithm with unsupervised ANN. This advancement signifies a new

and unique contribution to the discipline, as it establishes a foundation for subsequent efforts to resolve complex fractional order nonlinear partial differential equations (PDEs) by utilizing this hybrid ANN-based cuckoo search method. By employing this technique, it becomes possible to investigate and assess the temperature distribution and temperature at the tips of convective radial fins that possess thermal conductivity. This provides significant knowledge even when subjected to conditions of varying physical parameters. By combining unsupervised ANNs with the cuckoo search algorithm, the fractional order energy balance equation not only gives us better performance but also a new concept for complex problems in heat transfer and related domains. Significantly superior to traditional analytical methods, this hybrid scheme reduces computation time and data requirements in comparison to supervised ANN, thereby offering a more effective resolution for intricate heat transfer challenges.

2. Basic definitions

There are several definitions of fractional integrals and derivatives in fractional calculus, including Caputo, Riemann Liouville [41]. Following are some of the famous fractional integrals.

2.1. Definition

Suppose that $\theta \in H^1(a, b)$, where $a > b$ and $\beta \in [0, 1]$ then, as per Caputo, we have

$$\substack{C \\ 0} D_\xi^\beta \theta(\xi) = \frac{1}{\Gamma(m - \beta)} \int_0^z (\xi - \tau)^{m-\beta-1} [\theta'(\xi)] \mathrm{d}\tau.$$

We utilized the Riemann-Liouville formulation of fractional derivatives with a lower terminal at zero in our study. In the literature, the fractional order Riemann-Liouville derivative is defined as:

$$L\left[{}^{RL}D^\nu f(t)\right] = \frac{1}{\Gamma(m - \nu)} \frac{d^m}{dt^m} \int_0^t \frac{f(\tau)}{(t - \tau)^{1+\nu-m}} d\tau (m - 1 < \nu \leq m), \tag{2.1}$$

here, f is continuous, $\nu \in \mathbb{R}$, $n \in \mathbb{N}$ and Γ function is defined as under

$$\Gamma(x) = \int_0^\infty e^{-t} t^{x-1}, \mathcal{R}(x) > 0. \tag{2.2}$$

The Mittag-Leffler function (MLF) is significant. It has a wide range of applications in the field of fractional calculus. Its significance is recognized when solving fractional-order differential equations. Podlubny [41] provides the function with two arguments α and β as:

$$E_{\alpha,\beta}(t) = \sum_{k=0}^\infty \frac{t^k}{\Gamma(\alpha k + \beta)}, (\alpha > 0, \beta > 0), \tag{2.3}$$

and when we take $\beta = 1$, we have the standard MLF function for one parameter.

3. Problem formulation

Figure 1 shows a schematic picture of a straight fin issue with an arbitrary cross-sectional area, A_c, perimeter P, and length b. The fin is connected to the base surface with temperature, T_b, and extends into fluid with temperature, T_a, with its tip insulated.
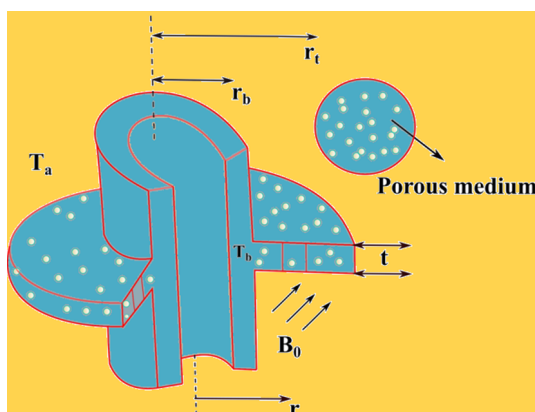
Figure 1. Geometrical description of the problem.

The energy balance equation is thus expressed as follows:

$$qr - q_{dr} = h^*(1 - \psi)(T - T_a)2\pi r + 2\pi r\psi\frac{\rho c_p gK\gamma}{v_f}(T - T_a)^2 + \frac{J_c^2}{\sigma}2\pi rt - 2\pi rtQ^*, \quad (3.1)$$

here Eq (3.1), q denotes the rate of heat transfer which is governed by the Fourier's law of heat conduction which is stated as follows:

$$q_r = -2\pi rtk_{eff}dT/dr, \quad (3.2)$$

calculating Eqs (3.1) and (3.2), the following relation is obtained:

$$\frac{d}{dr}\left(2\pi rtk_{eff}\frac{dT}{dr}\right) = h^*(1 - \psi)(T - T_a)2\pi r + 2\pi r\psi\frac{\rho c_p gK\gamma}{v_f}(T - T_a)^2 + \frac{J_c^2}{\sigma}2\pi rt - 2\pi rtQ^*. \quad (3.3)$$

In the above Eq (3.3), r and ψ represents the fin radius and porosity and the temperature dependent terms Q^* and h^* are denoted as [42]:

$$Q^*(T) = Q_q[1 + \lambda(T - T_a)],$$
$$h^*(T) = h_b\left[\frac{T - T_a}{T_b - T_a}\right]^p. \quad (3.4)$$

When applied at an angle of α, an inclined magnetic field with strength B_0 has the following mathematical expression [43]:

$$\frac{J_c^2}{\sigma} = \sigma B_0^2 \sin^2(\alpha)u^2. \quad (3.5)$$

The above Eq (3.3) can be defined as follows by applying the preceding equations:

$$\frac{d}{dr}\left(2\pi rtk_{eff}\frac{dT}{dr}\right) - h^*(1 - \psi)(T - T_a)2\pi r - 2\pi r\psi\frac{\rho c_p gK\gamma}{v_f}(T - T_a)^2$$
$$-2\pi rt\sigma B_0^2 \sin^2(\alpha)u^2\left[\frac{T-T_a}{T_b-T_a}\right]^p + 2\pi rtQ^*. \quad (3.6)$$

Additionally, the fin's energy transfer equation (Eq (3.6)) has the following boundary constraints [44]:

$$T(r_b) = T_b,$$
$$\frac{dT}{dr}\bigg|_{r=rt} = 0.$$

(3.7)

The following similarity phrases are required for the suggested problem:

$$\Theta = \frac{T}{T_b}, \quad \Theta_a = \frac{T_a}{T_b}, \quad \omega = \lambda(T_b), \quad R = \frac{r}{r_b}, N_C = \frac{h_b r_b^2}{k_{eff}t}, \quad M = \frac{\sigma B_0^2 u^2 r_b^2}{k_{eff}(T_b - T_a)},$$
$$Q = \frac{Q_a r_B^2}{k_{eff}T_b}, \quad S_H = \frac{\rho c_p g K \beta r_b^2 T_b}{v_f t k_{eff}}.$$

(3.8)

Using the appropriate similarity terms mentioned above, we obtain the dimensionless form of Eq (3.6):

$$\frac{1}{X}\frac{\mathrm{d}}{\mathrm{d}X}\left(X\frac{\mathrm{d}\Theta}{\mathrm{d}X}\right) - \mathrm{Nc}(1-\varphi)\frac{(\Theta - \Theta_a)^{p+1}}{(1-\Theta_a)^p} - S_H\varphi(\Theta - \Theta_a)^2$$
$$- M\sin^2(\alpha)(\Theta - \Theta_a) + Q[1 + \omega(\Theta - \Theta_a)] = 0,$$

(3.9)

together with the boundary conditions

$$\frac{d\Theta(0)}{dX} = 0, \qquad \Theta(1) = 1,$$

(3.10)

where X represent the dimensionless porous radius, the magnitude of p is picked between -3 and 3, as it characterizes the mechanism of energy transfer in most significant applications, including material processing, and nuclear reactions. Since, we know that integer order derivatives are local in nature, these derivatives cannot correctly characterize the situation. Because its kernel is non-local and non-singular, the Riemann-Liouville fractional derivative is more suited to describing natural occurrences. As a result, we substitute the second-order derivative in equation with the novel Riemann-Liouville fractional derivative, and this Eq (3.9) changes to a fractional model of energy balance equation written as:

$$\frac{1}{X}\frac{\mathrm{d}^\beta}{\mathrm{d}X^\beta}\left(X\frac{\mathrm{d}\Theta}{\mathrm{d}X}\right) - \mathrm{Nc}(1-\varphi)\frac{(\Theta - \Theta_a)^{p+1}}{(1-\Theta_a)^p} - S_H\varphi(\Theta - \Theta_a)^2$$
$$- M\sin^2(\alpha)(\Theta - \Theta_a) + Q[1 + \omega(\Theta - \Theta_a)] = 0.$$

(3.11)

While the boundary conditions remain the same.

4. Modeling with ANN and the optimization problem

The solutions to nonlinear problems are well studied in the literature, where various numerical and semi-analytical techniques are explained. The purpose behind the approximation of a solution for a mathematical relation is to find the best approximation that satisfies the given physical system more closely. To achieve this, we need to consider an efficient optimization algorithm. For this purpose, we introduce a feed-forward neural network approach for the fractional order problem (3.9) as follows:

$$\hat{\theta}(t) = \sum_{i=1}^{m} \xi_i\left[f(\delta_i t + \beta_i)\right],$$

(4.1)

$$\frac{d^\beta \hat{\theta}(t)}{dt^\beta} = \sum_{i=1}^{m} \xi_i \frac{d^\beta}{dt^\beta}\big[f\left(\delta_i t + \beta_i\right)\big], \tag{4.2}$$

here, δ, β, ξ are the ANN weights, m is the number of neurons, $f(t) = \exp(-t)$ is the sigmoid function, and $\hat{\theta}(t)$ is the approximate solution.

Based on the previous analysis, we assume an objective function $\mathcal{E}$ to reduce the L_2 norm for Eq (3.9). From above, we have

$$Minimize \qquad \mathcal{E} = \mathcal{E}_1 + \mathcal{E}_2, \tag{4.3}$$

where,

$$\mathcal{E}_1 = mean\Big[\frac{1}{X}\frac{d^\beta}{dX^\beta}\Big(X\frac{d\hat{\theta}_j}{dX}\Big) - Nc(1-\varphi)\frac{\big(\hat{\theta}_j - \hat{\theta}_{aj}\big)^{p+1}}{\big(1-\hat{\theta}_{aj}\big)^{p}} - S_H\varphi\big(\hat{\theta}_j - \hat{\theta}_{aj}\big)^2 - M\sin^2(\alpha)\big(\hat{\theta}_j - \hat{\theta}_{aj}\big) + Q\big[1 + \omega\big(\hat{\theta}_j - \hat{\theta}_{aj}\big)\big]\Big]^2 \tag{4.4}$$

and

$$\mathcal{E}_2 = mean\Big[(\hat{\theta}_1 - 1)^2 + (\hat{\theta}'_0)^2\Big]. \tag{4.5}$$

Here, $\xi_j = jh$, $\hat{\theta}_j = \hat{\theta}(\xi_j)$, $N = \frac{1}{h}$ where h shows the step size and $\xi \geq 0$. The whole mechanism of ANN is described in Figure 2.
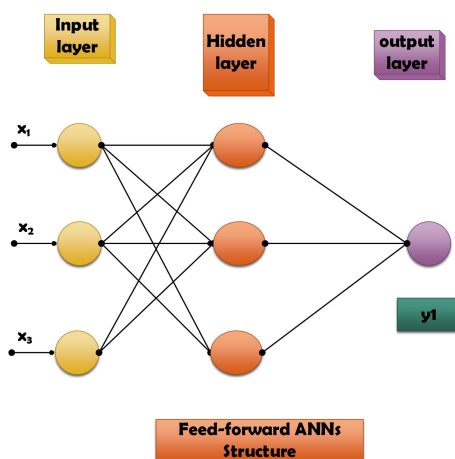

Figure 2. Geometrical description of the ANN for the fractional-order fin temperature model.

5. The Cuckoo search algorithm and its hybridization

As clear from the name Cuckoo, this algorithm uses the Cuckoo search (CS) strategy for finding the nest to lay their eggs there. The total search process follows the Lévy flights and random search approach. In some algorithms, like PSO and GA the local optima escapes, and the beauty of this search is that the local optima can not be escaped.

This algorithm follows the given search path

$$z_i^{t+1} - z_i^t = \alpha s \otimes H\big(p_a - \epsilon\big) \otimes \big(z_j^t - z_k^t\big). \tag{5.1}$$

The Lévy walk equation further enhances the global search for z_i^{t+1}. Here, $H(u)$ is the Heaviside function, z_i^{t+1} and z_i^t are the two separate roots, p_a represents the changing parameter, ϵ is the random

variable, $s > 0$ is the size of the step taken, $\otimes$ is the element-wise product, and α is the scaling parameter.

The CS algorithm can be further optimized with the Biogeography-based operator. In this methodology, these modified operators are used to build a new optimal solution based on hybrid Cuckoo search (HCS). In the search phase, the host bird is allowed to find the other Cuckoo eggs with higher accuracy to remove the old or to adopt it based on the optimal condition. The total population is again re-evaluated and the rate of emigration μ is chosen for each response. This rate can be defined as:

$$P\mu_i = \frac{ES_i}{M}, \tag{5.2}$$

here, $E = 1$ shows the maximum rate of emigration and $Si = MPI$ is the solution of the species chosen. The total mechanism of the proposed methodology is explained in Figure 3.
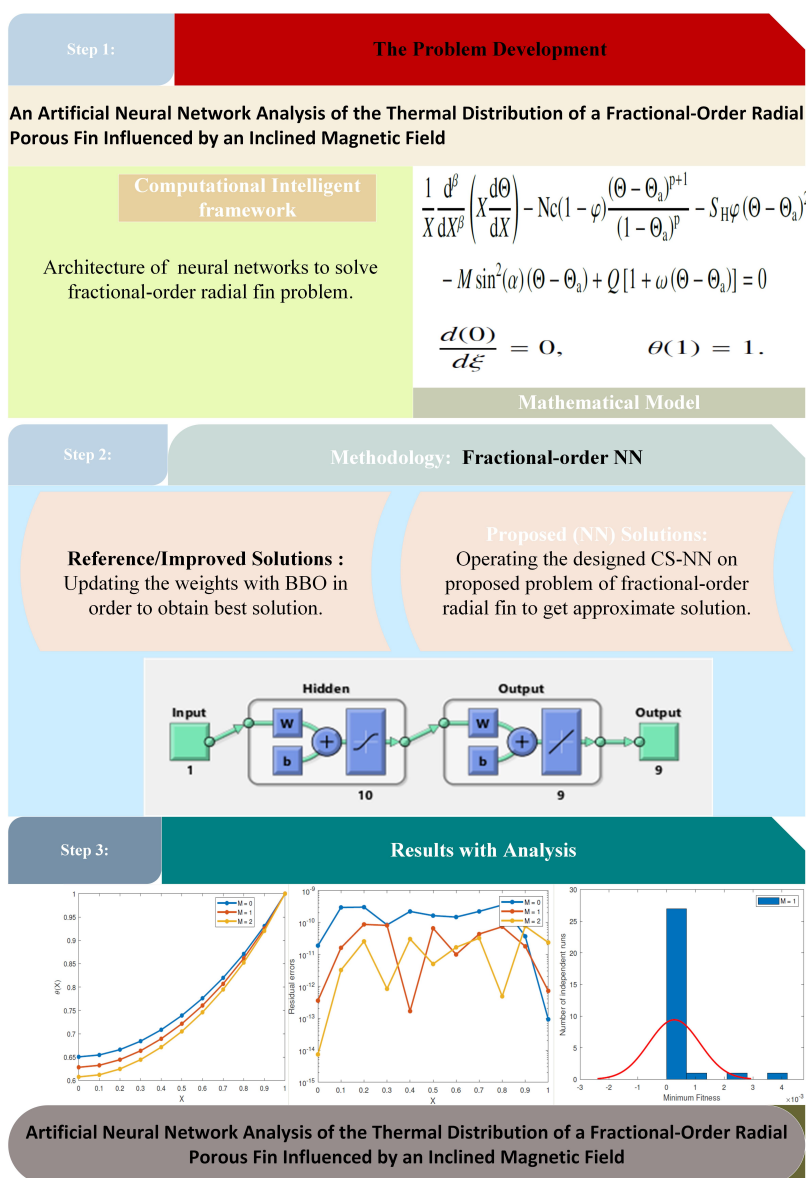

Figure 3. Description of the work to execute the problem efficiently.

6. Results and discussions

I) Variations of Fractional order $\beta = (1, 0.9, 0.8, 0.7)$, Hartmann number $M = (0, 1, 2)$ and Temperature ($\theta(\eta)$): Figures 4–7 (a) and (b). The parameters for the graphs in Figures 4–7 are kept as $M = (0, 1, 2), \beta = (1, 0.9, 0.8, 0.7), Q = 0.2, \omega = 0.1, S_H = 0.8, \Theta_a = 0.2, N_c = 2, \alpha = \pi/6$. Varying the values of $M = (0, 1, 2)$ in each Figure 4–7 and every trial have 30 runs for a different fractional order i-e for $\beta = (1, 0.9, 0.8, 0.7)$, different in every case, while the other parameters remain constant in each trial.

• Figure 4 (a) and (b)

The solution plot of the Hartmann number (M) and $\beta = 1$ and the non-dimensional temperature (θ) is illustrated in Figure 4(a). a dimensionless parameter that defines the intensity of a magnetic field that is exerted on a fluid with electrical conductivity. The graph demonstrates that as (M) increases, there is a concomitant increase in temperature (θ). The observed outcome can be ascribed to the Lorentz force produced by the magnetic field, which opposes the flow of the fluid and causes a rise in temperature. Furthermore, the graph visually represents the progression of temperature (θ) in relation to (M), underscoring that the Lorentz force becomes more pronounced as the strength of the magnetic field increases. The plot was generated utilizing the Hybrid Cuckoo Search algorithm, which is a neural network technique.

• The parameters for the graphs in Figures 4–7 are kept as $\beta = (1, 0.9, 0.8, 0.7), Q = 0.2, \omega = 0.1, S_H = 0.8, \Theta_a = 0.2, N_c = 2, \alpha = \pi/6$. Varying the values of M=0,1,2 in each Figures 4–7 and every trial have 30 runs for a different fractional order i-e for $\beta = (1, 0.9, 0.8, 0.7)$, different in every case, while the other parameters remain constant in each trial.

The visual depiction emphasizes the substantial influence that the Hartmann number has on the temperature of the system. A stronger Lorentz force results from a more pronounced magnetic field, which is denoted by an increased number (M). This force, which acts in opposition to the fluid's flow, causes the temperature to rise. The graph in Figure 4(b) depicts the residual errors that arise from temperature variations for various values of M (0, 1, 2). The defects, which occur within a specified range for every value of M, serve as an indication of the fractional order β residual in this case lie between 10^{-9} and 10^{-14}. Residual errors, also known as residuals, are mathematical or statistical discrepancies that arise from the opposition between predicted and observed values.

The computation involves the subtraction of predicted values from observed values. Critical for determining whether a model fits its data and for detecting patterns, trends, and outliers is residual analysis. Residuals ought to be centered on zero and distributed at random, which would indicate that the model has captured the underlying data patterns. In disciplines such as statistics, economics, finance, and machine learning, residual analysis is utilized to assess the performance and dependability of predictive models. The insights gained from this analysis regarding the behavior of the system and the influence of fractional orders on temperature fluctuations are of great value.
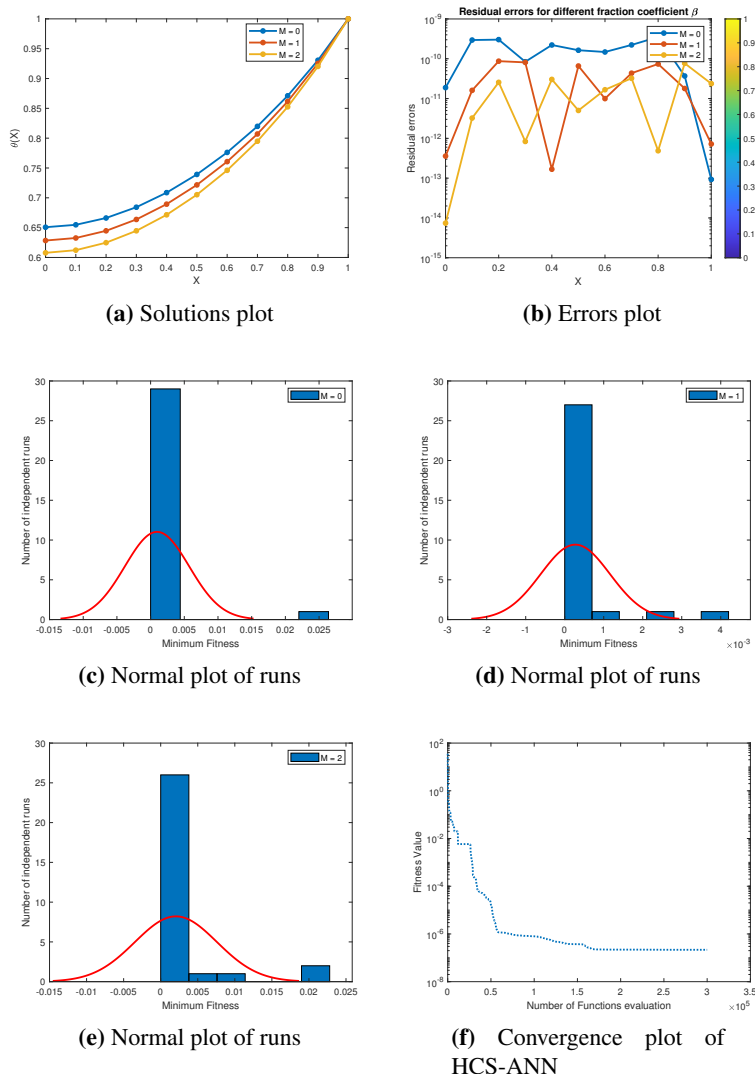
(a) Solutions plot

(b) Errors plot

(c) Normal plot of runs

(d) Normal plot of runs

(e) Normal plot of runs

(f) Convergence plot of HCS-ANN

Figure 4. Graphical results obtained with variation in $M = 0, 1, 2$ with fractional-order $\beta = 1$.

• Figure 5 (a) and (b)

The relationship between the Hartmann number (M = 0, 1, 2) and the non-dimensional temperature is depicted in the solution plot of Figure 5(a). This non-dimensional temperature parameter defines the electrical conductivity-induced effect of a magnetic field on a fluid. The results of the analysis underscore the significance of the Lorentz force in this phenomenon and the impact of the Hartmann number on temperature, as illustrated by the Hybrid Cuckoo Search algorithm. The implications of these findings f The temperature variation (θ) as the Hartmann number (M) increases is graphically represented in the graph. An increase in the Hartmann number is correlated with a proportional rise in temperature, as indicated by the observed trend. The observed behavior can be ascribed to the Lorentz force produced by the magnetic field, which acts in opposition to the flow of fluid and causes an increase in temperature. By generating the solution plot, the Hybrid Cuckoo Search algorithm demonstrates its effectiveness in optimizing the system parameters. Using fractional order β, the parameters for the diagrams in Figure 5(a) are maintained. By manipulating β from 1 to 0.9, the graph investigates the effect of fractional order on temperature (θ) in greater detail.

Significantly, a reduction in fractional order is accompanied by a corresponding decrease in temperature, as is evident from Figure 5(a). The incremental improvement of values as β decreases underscores the fractional order sensitivity of the system. In brief, the graph adeptly illustrates the intricate relationship that exists among the Hartmann number, fractional order, and temperature with respect to the influence of a magnetic field on a fluid system. The residual errors caused by temperature variations for various M values are illustrated in Figure 5(b), which represent fractional order defects. Mathematical or statistical disparities between predicted and observed values constitute residuals. They ought to be random and equal to zero, which would indicate model accuracy. These Residuals errors fall between 10^{-6} and 10^{-14}. In disciplines such as statistics, economics, finance, and machine learning, residual analysis is utilized to evaluate the efficacy of predictive models and the behavior of systems.
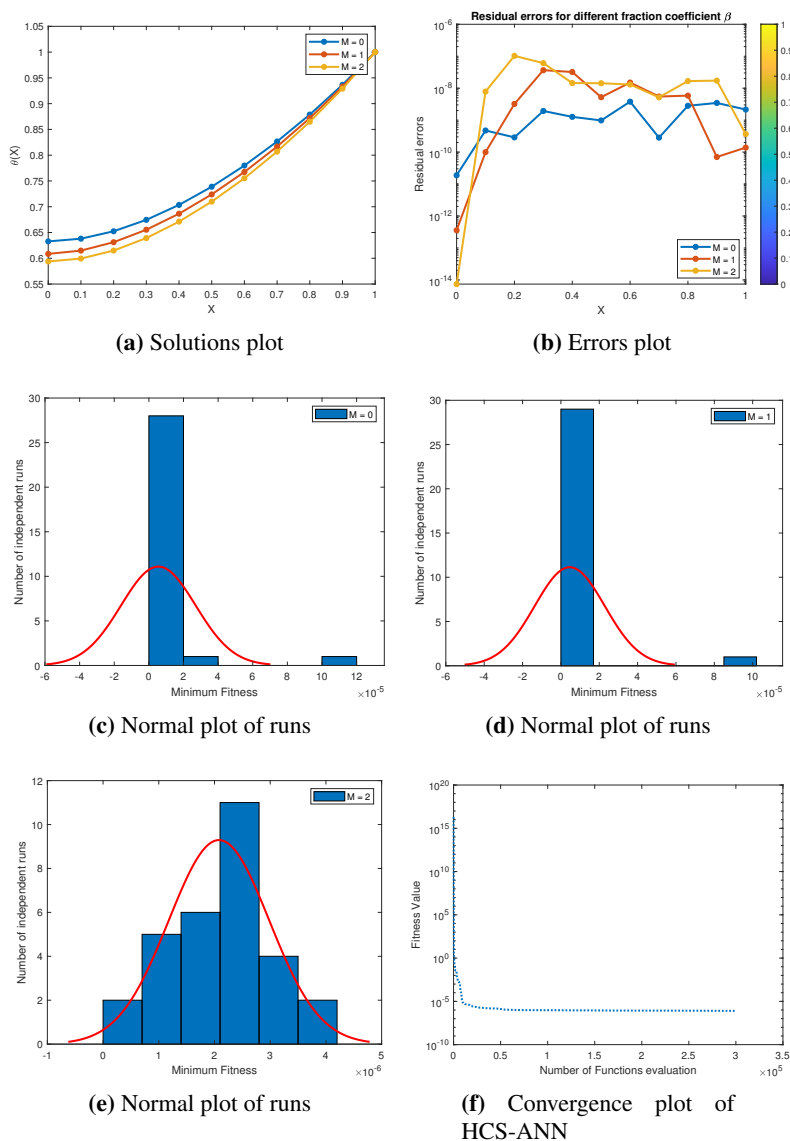

(a) Solutions plot

(b) Errors plot

(c) Normal plot of runs

(d) Normal plot of runs

(e) Normal plot of runs

(f) Convergence plot of HCS-ANN

Figure 5. Graphical results obtained with variation in $M = 0, 1, 2$ with fractional-order $\beta = 0.9$.

(a) Solutions plot

(b) Errors plot

(c) Normal plot of runs

(d) Normal plot of runs

(e) Normal plot of runs

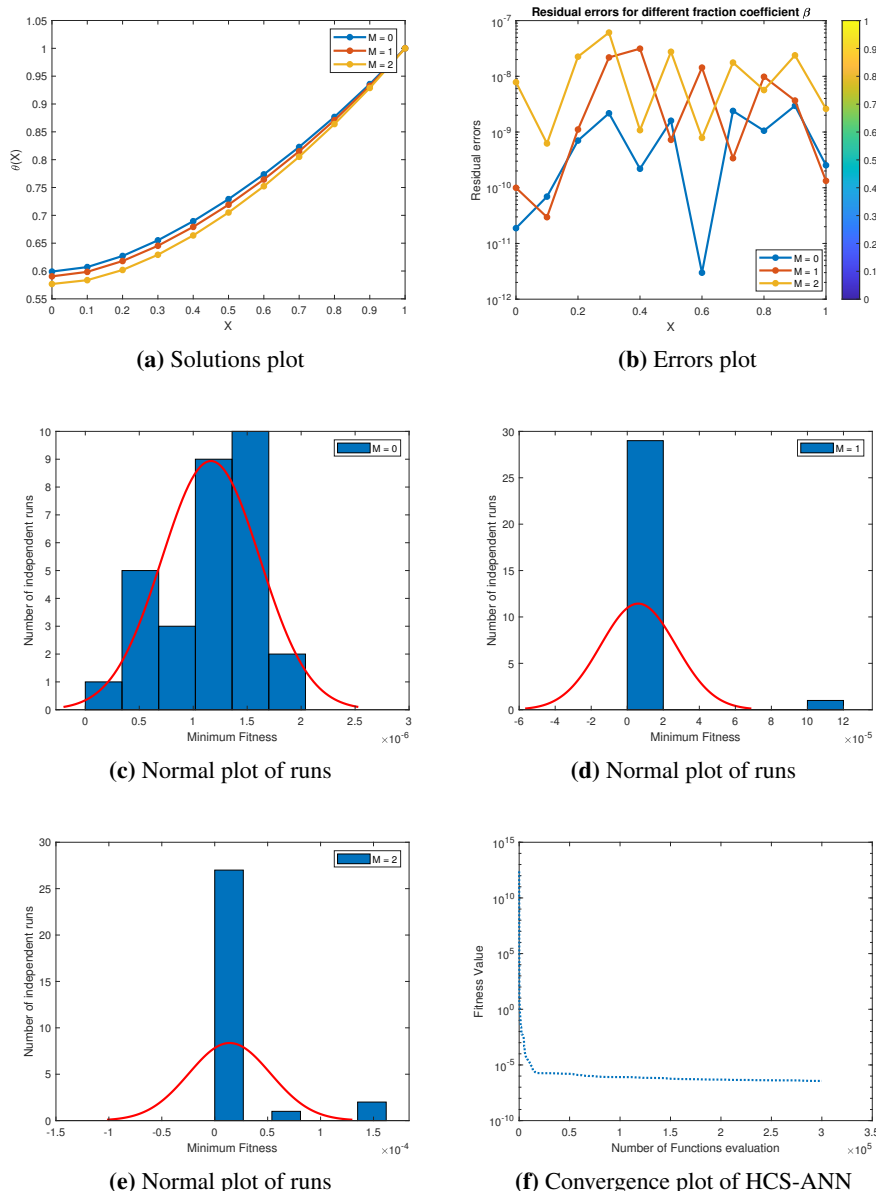**(f)** Convergence plot of HCS-ANN

Figure 6. Graphical results obtained with variation in $M = 0, 1, 2$ with fractional-order $\beta = 0.8$.

- Figure 6 (a) and (b)

This research investigates the correlation between non-dimensional temperature and the Hartmann number (M = 0, 1, 2), with a particular emphasis on the Lorentz force and its influence on temperature, shown in Figure 6(a). The efficacy of the Hybrid Cuckoo Search algorithm in identifying temperature variation is demonstrated by its use in optimizing system parameters. The Figure 6(a), illustrates a positive correlation between temperature and Hartmann number, which can be attributed to the Lorentz force generated by the magnetic field. Additionally, the fractional order sensitivity of the system is emphasized. The fractional order is employed to preserve the parameters of the diagrams shown in Figure 6(a). By manipulating from 1 to 0.9 and then 0.8, the graph provides a more comprehensive

examination of the impact that fractional order has on temperature (θ). Unsurprisingly, a decrease in temperature corresponds to a reduction in fractional order, as illustrated in Figure 6(a).

Residual errors associated with temperature fluctuations for different values of M are illustrated in Figure 6(b). Residuals are quantified as discrepancies from the anticipated values that fall within a designated range. The residual errors are identified to be concentrated between 10^{-7} and 10^{-12}. The defined range facilitates comprehension of the extent to which actual values deviate from predictions. Residuals function as a numerical indicator of the discrepancies that exist between anticipated and realized values. Residuals are anticipated to be random and centered on zero in an accurate model, signifying a negligible margin of error in the predictions. Its significance is paramount in assessing the efficacy of predictive models and comprehending the behavior of systems. The residual errors illustrated in Figure 6(b) provide significant insights into the fractional order defects that are linked to fluctuations in temperature for various values of M. The range of residuals that has been established is utilized to evaluate the precision of the predictive model and the magnitude of errors.

- Figure 7 (a) and (b)

A continuance of the fractional order reduction from $\beta = 1$ to $\beta = 0.7$ for different values of the Hartmann number M is illustrated in Figure 7(a). As a consequence of this decrease, temperature values are likewise reduced in comparison to the preceding three instances The reduction in fractional order from $\beta = 1$ to $\beta = 0.7$, for $M = 0, 1$, and 2 is visually represented in Figure 7(a), The graph visually represents the subsequent decrease in temperature measurements. The observed decrease in value occurs at M = 0, 1, and 2, underscoring the impact that fractional order has on the temperature response of the system. The graph highlights the degree of sensitivity that the system exhibits towards fractional order alterations. Comprehending this sensitivity is of the utmost importance in order to optimize system parameters and accurately forecast temperature fluctuations. This graphical representation facilitates the understanding of the complex correlation between temperature, M values, fractional order, and the former, thereby providing practitioners and researchers with valuable insights for optimizing systems and fine-tuning parameters. Residual errors, shown in Figure 7(b), which are measured as differences between expected and observed values, are critical for evaluating the effectiveness of predictive models and comprehending the behavior of systems. The residual errors are identified to be concentrated between 10^{-7} and 10^{-11}. They are inter-concentrated. In an accurate model, residuals are anticipated to be zero and at random, signifying a minimal margin of error. The range of residuals is utilized to assess the precision and magnitude of the model's error.

When the magnetic field angle varies, the Hartmann number rises and the rate of heat transfer increases. A decrease in temperature results from increasing the Hartmann number from 2 to 3. As M values increase, the magnetic influence and corresponding magnetization strength increase as well, regulating convective heat transfer and increasing the fin's average heat transmission. Moreover, the buoyancy force is triggered by the magnetic field, which permits the fin to disperse additional heat. Consequently, there is an acceleration of the heat transfer rate from the fin. The feature of thermal distribution in the radial porous fin with and without magnetic field is exhibited in Figures 4–7. The temperature distribution in the fin with a magnetic field inclined at an angle of $\pi/6$ is indicated by the lower curve of the thermal profile, whereas the higher temperature curve is observed in the absence of a magnetic field. This suggests that fins with an angled magnetic field transmit heat at a faster rate. Additionally, there is a difference in these two curves. Physically, a magnetic field and the magnetic force that it attracts restrict the convection heat transport process, increasing the average

heat transmission through the fin. This relationship is applied in the construction of nuclear reactors, where efficient heat removal is necessary to prevent overheating. The impact of the Hartmann number, a fundamental feature of electrically conducting fluids used as reactor coolants, must be carefully considered in the design of the cooling system to ensure the safe and effective operation of nuclear reactors.
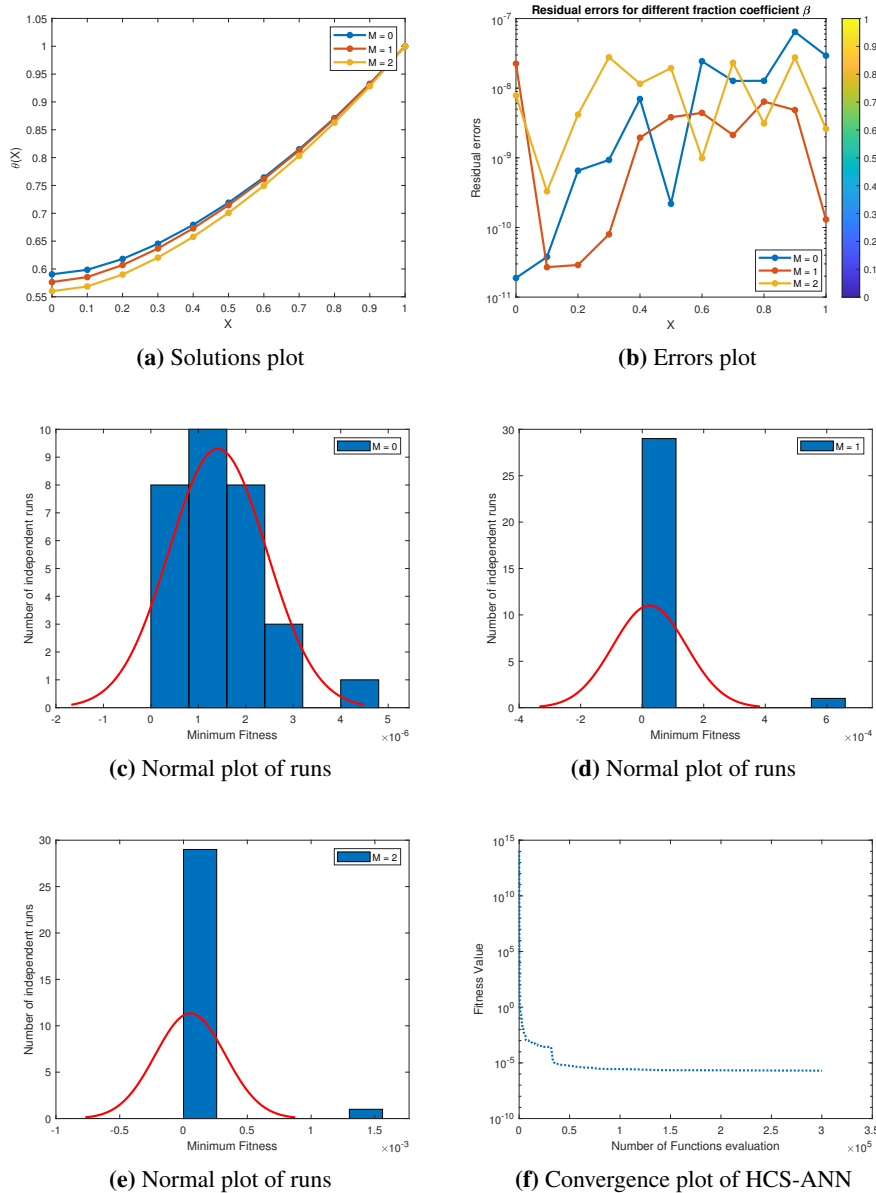

(a) Solutions plot

(b) Errors plot

(c) Normal plot of runs

(d) Normal plot of runs

(e) Normal plot of runs

(f) Convergence plot of HCS-ANN

Figure 7. Graphical results obtained with variation in $M = 0, 1, 2$, with fractional-order $\beta = 0.7$.

(a) Solutions plot

(b) Errors plot

(c) Normal plot of runs

(d) Normal plot of runs

(e) Normal plot of runs

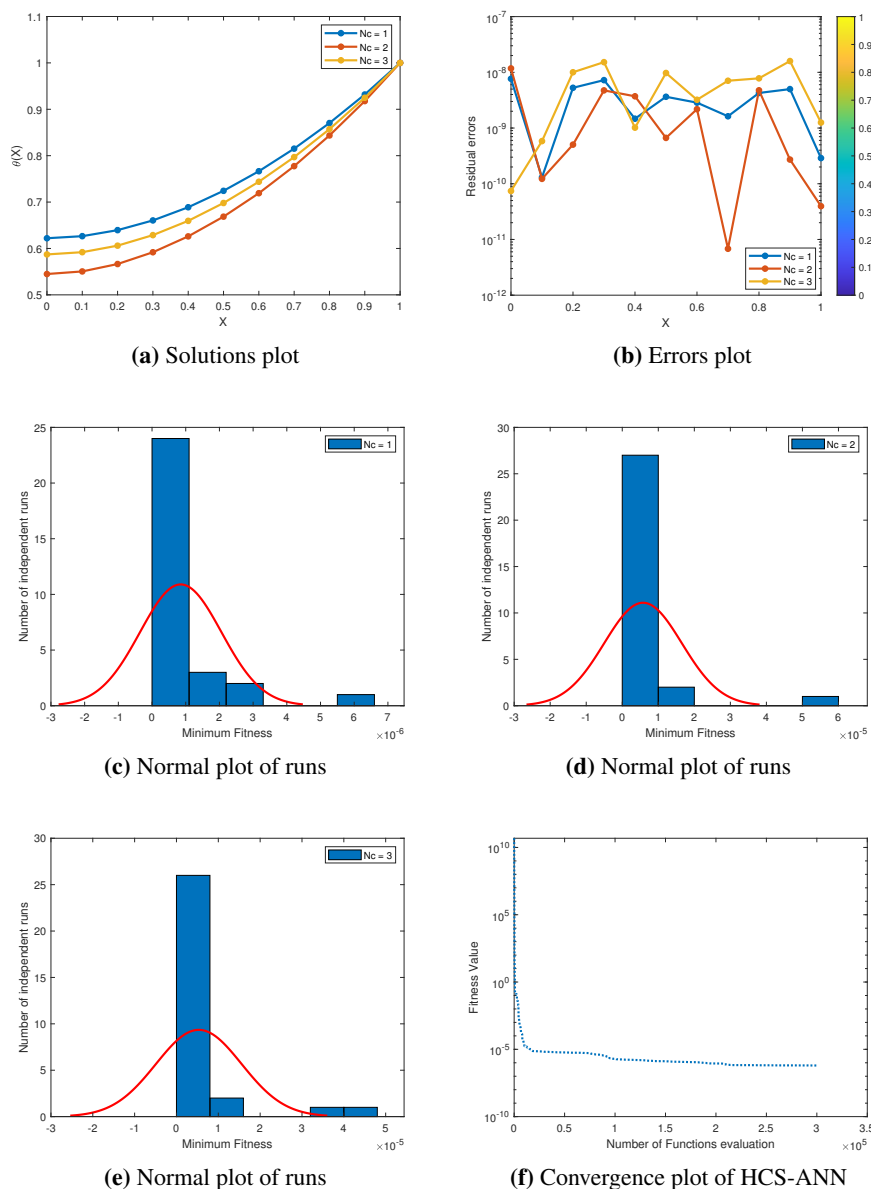**(f)** Convergence plot of HCS-ANN

Figure 8. Graphical results obtained with variation in $M = 0, 1, 2$ with fractional-order $\beta = 1$.

II) The fitness curves for the HCS deep ANN are illustrated in Figures 4–7 (c)–(e). These curves highlight the impact of the M Hartmann number on performance, with specific attention paid to M values of zero, one, and two. The minimal fitness values are represented along the x-axis, whereas the outcomes of 30 independent runs of HCS deep ANN are depicted on the y-axis. The focus of the analysis is a fractional orders $\beta = 1, 0.9, 0.8, 0.7$.

Crucial observations:

• M = 0 and $\beta = 1$: Figure 4(c)

The fitness curve demonstrates variability spanning from -0.0015 to $+0.0015$, with its maximum value occurring approximately 12 independent runs in advance. It then descends until it reaches a stability at 0.0015. The HCS deep ANN exhibits remarkable performance even in the absence of the

M Hartmann number and the fractional order $\beta = 1$.

• M = 1 and $\beta = 1$: Figure 4(d)

The fitness curve exhibits a conspicuous flattening in comparison to the condition where M=0, which indicates a substantial influence of the M Hartmann number. It peaks around the tenth run independently and then declines progressively. The presence of an optimal value for the M Hartmann number indicates that it plays a pivotal role in optimizing the performance of the HCS deep ANN.

• M = 2 and $\beta = 1$: Figure 4(e)

The fitness curve exhibits a behavior that is flatter than that of M = 0 and M = 1. It reaches its maximum after eight independent trials, after which it gradually decreases until it stabilizes at 0.02. Although M = 2 is flatter than M = 0 and M = 1, its fitness is marginally lower, highlighting the subtle influence of the M Hartmann number.

In conclusion, the aforementioned observations highlight the performance of the HCS deep ANN being highly susceptible to fluctuations in the M Hartmann number. The results of the analysis indicate the presence of an ideal M value, and the fractional order (β) remains unchanged at 1 for the duration of the investigations.

• M = 0 and $\beta = 0.9$: Figure 5(c)

A dynamic pattern is observed in the fitness curve for M=0 and $\beta = 0.9$. It fluctuates initially between -6×10^{-5} and -7×10^{-5}, peaking after 12 independent cycles. Following this, a significant decrease occurs, culminating in a value of -7×10^{-5} for $\beta = 0.9$, which signifies resilient performance even in the absence of the M Hartmann number. This implies that the HCS deep ANN attains an impressive level of fitness that is not influenced by the M Hartmann number.

• The fitness curve for the conditions M = 1 and $\beta = 0.9$ shown in Figure 5(d), exhibits a significant enhancement in comparison to the curve for M = 0. Following the attainment of the peak after approximately 12 independent trials, the curve begins to decline. The values fall between -5×10^{-5} and 6×10^{-5}. The fitness values, demonstrate the influence of M=1 and the importance of the fractional order $\beta = 0.9$. The possibility of an optimal M Hartmann number in this particular situation is indicated by the decrease in fitness subsequent to attaining the maximum.

• M = 2 and $\beta = 0.9$: Figure 5(e)

The fitness curve for M = 2 and $\beta = 0.9$ is marginally inferior to those for M = 0 and M = 1. The value reaches its maximum after nine distinct iterations, after which it descends. For M = 2 and $\beta = 0.9$, the fitness values fall within the interval of -1×10^{-6} and 5×10^{-6}, suggesting an enhanced level of performance in comparison to alternative situations.

The decrease in value signifies the attainment of a stable solution, demonstrating enhanced performance for the particular amalgamation of the M Hartmann number and fractional order. In brief, the fitness curves demonstrate the degree of responsiveness of the HCS deep ANN algorithm to variations in the M Hartmann number and β values. This underscores the importance of investigating optimal configurations in order to enhance performance when addressing the provided problem. The fitness curves presented in Figure 6 (c)–(e) offer an exhaustive depiction of the behavior of the HCS-ANN algorithm in various M Hartmann number scenarios.

Figure 6 (c)–(e): Evaluation • M = 0 and $\beta = 0.8$: Figure 6(c)

In the absence of M. Hartmann, the robustness fitness curve exhibits a dynamic pattern, reaching its maximum after approximately 9 independent trials, shown in (Figure 6(c)). The dynamic nature of the algorithm is underscored by the fitness values that span the range of and. Notwithstanding in

the absence of the M Hartmann number, the algorithm exhibits remarkable robustness by sustaining a significant level of fitness. The range of fitness values is from 1×10^{-6} and 1.5×10^{-6}. It is noteworthy that the algorithm retains a substantial degree of fitness despite the absence of the M Hartmann number, which demonstrates its resilience.

• M = 1 and $\beta = 0.8$: Figure 6(d)

When M = 1 and $\beta = 0.8$, the fitness curve reaches its maximum after approximately 11 independent trials, shown in Figure 6(d), which is greater than that of M=0. By situating the fitness values between -6×10^{-5} and 7×10^{-5}, one can discern that the implementation of the M Hartmann number has enhanced the algorithm's performance. In contrast to M=0, the curve's flattened profile indicates a more secure convergence. A post-peak decline indicates that the M Hartmann number has been searched for its optimal value, demonstrating that it has a substantial impact on the efficiency of the algorithm.

• M = 2 and $\beta = 0.8$: Figure 6(e).

When M = 2 and $\beta = 0.8$ Following nine independent trials, the fitness curve for M = 2 attains its optimum value. The fitness values, which lie between 1.5×10^{-4} and -1×10^{-4} exhibit superior performance compared to M=0 and M=1. This particular situation exemplifies the HCS-ANN algorithm at its highest level of performance; the efficacy is significantly enhanced by combining M=2 with the fractional order $\beta = 0.8$. Figure 6 (e) illustrates enhanced performance (M = 2, and $\beta = 0.8$) i-e After nine independent trials, the fitness curve for M = 2 reaches its maximum, surpassing the performance of M = 0 and M = 1.

Figures 7 (c)–(e): Evaluation

The fitness curves depicted in Figure 7 (c)–(e) offer significant insights regarding the HCS-ANN algorithm's performance across various scenarios in which the M Hartmann number is involved.

• Figure 7(c) illustrates the robustness when M Hartmann is absent (M = 0 and $\beta = 0.7$):

The fitness curve for M=0 exhibits a dynamic pattern, with its optimum value being attained after approximately nine independent trials. The robustness of the algorithm is underscored by the fitness values, which span from -2×10^{-6} to 4.5×10^{-6} , even in the absence of the M Hartmann number. The dynamic pattern indicates that the algorithm is robust, as it can adapt to a variety of conditions.

• M = 1 and $\beta = 0.7$: Figure 7(d)

The fitness curve reaches its optimum after approximately 12 independent trials for M = 1, surpassing that of M=0. Fitness values are typically observed between -3×10^{-4} to 4×10^{-10} , with a more gradual curve indicating a state of stability. The decline that occurs after the peak indicates that the M Hartmann number influenced an optimal value pursuit, demonstrating the algorithm's sensitivity to parameter variations. • Increased Performance (M = 2 and $\beta = 0.7$): Figure 7(e) The fitness curve for M = 2 reaches its optimum after 12 independent trials, outperforming M=0 and M=1. The fact that fitness values are constrained by 1×10^{-6} and 2.5×10^{-6}. suggests that the algorithm functions optimally when M equals 2 and the fractional order $\beta = 0.7$ is applied. This scenario exemplifies the algorithm's improved performance, as it reaches its maximum efficacy when particular parameter configurations are utilized. The intricate performance of the HCS-ANN algorithm in different scenarios involving the M Hartmann number is depicted in Figure 7 (c)–(e). To summarize, the resilience, responsiveness to optimal values, and optimum efficiency of the HCS-ANN algorithm across various scenarios involving the M Hartmann number are illustrated in Figure 7 (c)–(e). A comprehensive comprehension of the algorithm's behavior and performance is

obtained through the nuanced analysis.

- Convergence Figures 4–7 (f)

The fitness graphs generated by the HCS-ANN Deep Learning algorithm offer significant insights regarding its optimization performance and convergence characteristics. The fitness value is represented along the y-axis and the number of function evaluations is represented on the x-axis. The mean fitness value of the population is represented by the red line, whereas the fitness values of individual particles are illustrated by the blue lines. A thorough examination of the graph reveals the following significant observations: Achieving Optimal Solution Convergence: The efficient convergence of the Novel HCS-ANN algorithm is depicted in the graphs. The mean fitness value of the population stabilizes around function evaluations at approximately 10^{-6} for $\beta = 1$, 10^{-5} for $\beta = 0.9$, 10^{-5} for $\beta = 0.8$ and 10^{-5} for $\beta = 0.7$, around 3×10^{5} function evaluations shown in Figures 4–7 (f) respectively. This suggests that the algorithm possesses the ability to rapidly locate a solution that produces a desirable fitness value.

The convergence of individual particles is visually apparent in the clustering of blue lines around the red line. This indicates that the algorithm directs every particle towards the identical optimal solution, thereby enhancing the algorithm's consistency and dependability. Algorithm Efficiency: The Novel HCS-ANN algorithm is a robust and efficient optimization method, as indicated by the graph's overall trend. The rapid convergence towards optimal solutions serves as evidence of its effectiveness in resolving intricate optimization issues.

An Examination of Subfigures The fitness diagrams in Figures 4–7 (f) illustrate errors for the following scenarios: $\beta = 1, 0.9, 0.8$, and 0.7, respectively. The subfigures additionally illustrate the error distribution relative to the zero error line, which facilitates the evaluation of both accuracy and validity. An error value that is lower signifies enhanced precision and improved efficacy of the solution methodology. In summary, the fitness graphs and subfigures provide conclusive evidence supporting the effectiveness of the Novel HCS-ANN algorithm as a robust optimization instrument. The efficiency with which it converges to high-quality solutions and adjusts to various scenarios, as evidenced by its beta values, underscores its adaptability and dependability across a range of optimization tasks.

III) Variation of fractional order ($\beta = 1, 0.9, 0.8, 0.7$), Temperature (θ) and the convective–conductive parameter (Nc =(1,2,3)):

$N_c = (1, 2, 3), M = 3, (\beta = 1, 0.9, 0.8, 0.7), Q = 0.2, \omega = 0.1, \Theta_a = 0.1, \alpha = \pi/6.$

Varying the values of $Nc = 1, 2, 3$ in each Figure 8–11 and every trial have 30 runs for different fractional orders i-e for ($\beta = 1, 0.9, 0.8, 0.7$), different in every case, while the other parameters remain constant in each trial. Figures 8–11 (a) and (b): It is essential to analyze temperature, the convective-conductive parameter Nc, and fractional order beta in order to comprehend the system's behavior under various conditions. Determining meaningful conclusions is made possible by the insightful solution graphs and residual errors presented in Figures 8–11 (a) and (b) for varying parameters.
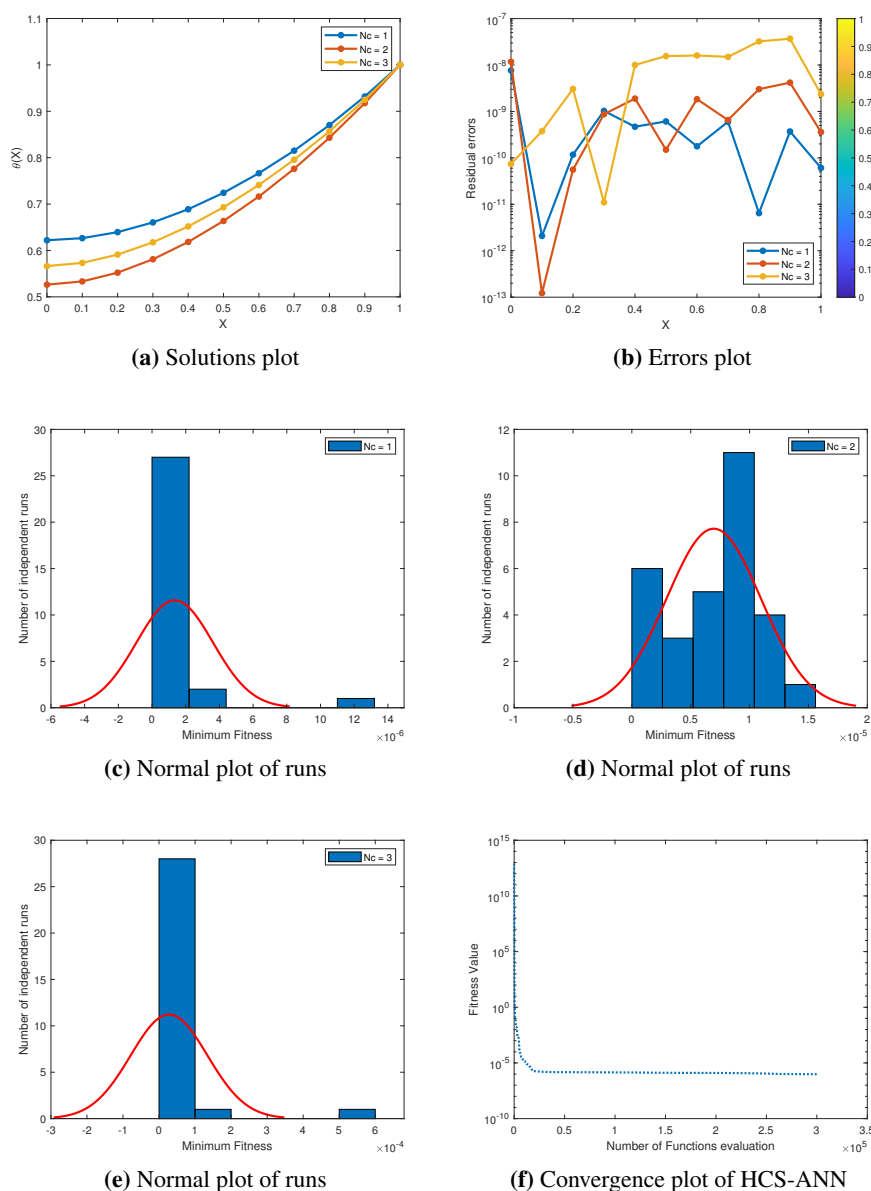
(a) Solutions plot

(b) Errors plot

(c) Normal plot of runs

(d) Normal plot of runs

(e) Normal plot of runs

(f) Convergence plot of HCS-ANN

Figure 9. Graphical results obtained with variation in $Nc = 1, 2, 3$ with fractional-order $\beta = 0.9$.

- The fluctuation of the convective-conductive parameter Nc is illustrated in Figure 8(a) when the fractional order β is set to 1. As Nc increases from 1 to 3, a distinct trend of decreasing temperature is observed. This observation implies that elevated values of Nc are associated with reduced temperatures, thereby establishing a robust inverse correlation between Nc and temperature. From these plots, the significance of Nc in influencing temperature dynamics is evident. The solution plot of temperature versus Nc is illustrated in Figure 9(a) for a β value of 0.9. Consistent with prior research, the observed pattern indicates that a rise in Nc results in a corresponding decline in temperature. This uniformity strengthens the correlation between Nc and temperature behavior.
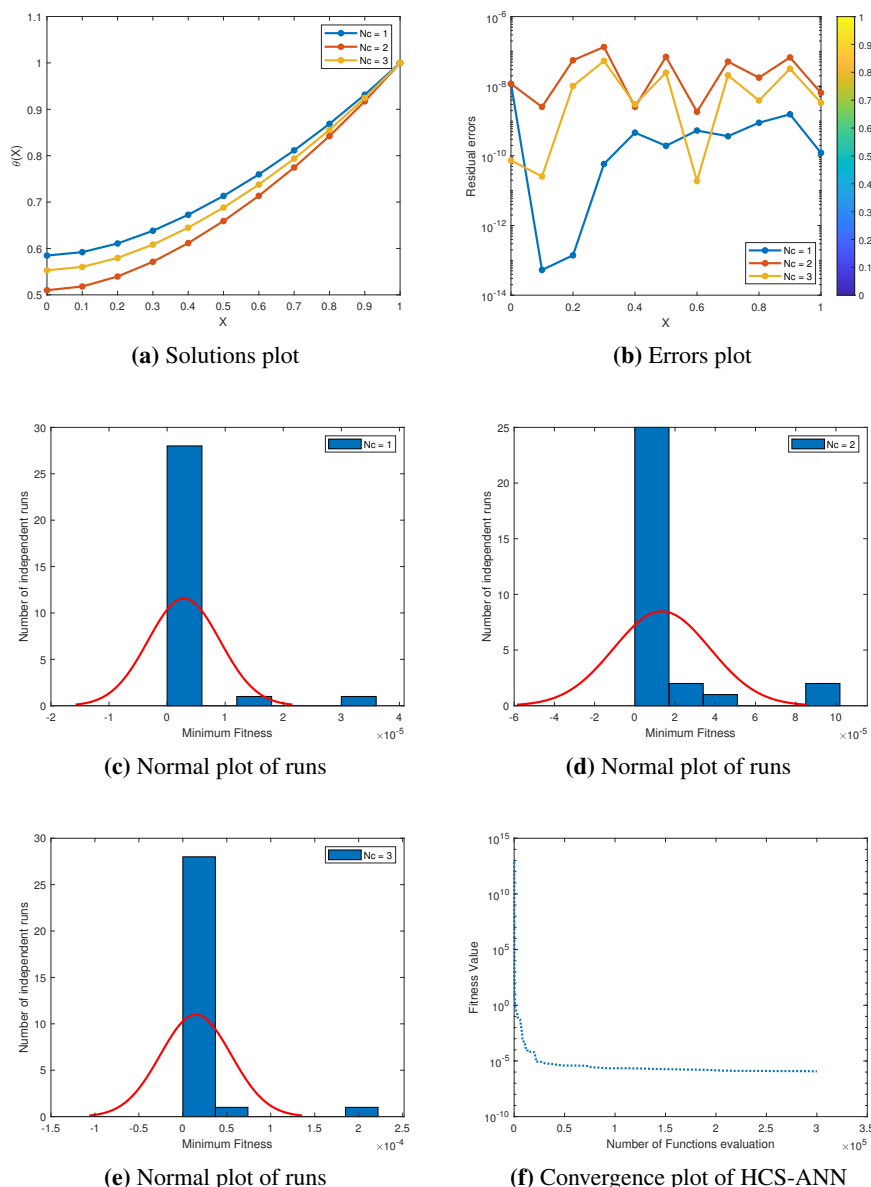
(a) Solutions plot

(b) Errors plot

(c) Normal plot of runs

(d) Normal plot of runs

(e) Normal plot of runs

(f) Convergence plot of HCS-ANN

Figure 10. Graphical results obtained with variation in $Nc = 1, 2, 3$ with fractional-order $\beta = 0.8$.

The influence of Nc on temperature is additionally examined in Figure 10 (a) and (b), specifically for β values of 0.8 and 0.7, respectively. In both instances, the temperature decreases as Nc increases from 1 to 3. This finding supports previous research and underscores the strong correlation between Nc and temperature when considering various fractional orders. It is important to highlight that the fractional order beta β is a crucial factor in influencing the dynamics of temperature. A reduction in temperature is equivalent to a decrease in the fractional order beta, as depicted in Figures 8–11 (a). This suggests that as fractional orders decrease, the resulting temperatures become more precise. A complete comprehension of the system's behavior requires an awareness of the temperature effect produced by Nc and β combined. In summary, the solution plots that were displayed underscore the

complex interaction that exists among Nc, fractional order beta β, and temperature. The insights gained from the observed trends regarding the effects of parameter variations on the thermal behavior of the system are of great value. Additional investigation and examination of these correlations may enhance our comprehension of the intricate physical mechanisms at play.

• In order to evaluate the performance of the HCS-ANN model under various conditions, particularly for distinct fractional orders (BETEA) and convective-conductive parameters (Nc), residual error analysis is critical. The residual errors for temperature corresponding to various values of Nc and β are depicted in Figures 8(b) and 9(b). The residual errors for fractional order beta equal to 1 and Nc values of 1, 2, and 3 are contained within the range shown in Figure 8(b). This finding suggests that the HCS-ANN model exhibits satisfactory performance under the given conditions. The limited extent of variation implies a consistent and dependable forecast for temperature in light of these conditions. The analysis is expanded to include fractional order beta equal to 0.9 and Nc values of 1, 2, and 3 in Figure 9(b). The residual errors are, which indicates that despite a minor reduction in fractional order, the model retains its accuracy. This further validates the HCS-ANN model's ability to accurately represent temperature variations when convective-conductive parameters are altered. The residual errors for fractional order beta equal to 0.8 and Nc values of 1, 2, and 3 are all within the acceptable range, as shown in Figure 10(b). Notwithstanding the reduction in fractional order and possible escalation in complexity, the model continues to demonstrate satisfactory performance, as errors continue to fall within an acceptable range. Finally, the residual errors for fractional order beta equal to 0.7 and Nc values of 1, 2, and 3 are illustrated in Figure 11(b). The range of residual errors is, indicates that the predictive capabilities of the HCS-ANN model are preserved even when convective-conductive parameters are higher and fractional order is lower.

• Figures 8–11 (c)–(e) Fitness plots.

Conducting an examination of the fitness curve produced by HCS-ANN with respect to various convective-conductive parameters (Nc) and fractional orders β is critical in order to assess the algorithm's performance and convergence characteristics. The minimum fitness range for 30 independent trials is illustrated in Figures 8–11 (c)–(e), providing valuable insights into the optimization process across different conditions.

• Nc = 1, 2 and 3 and $\beta = 1$ Figure 8 (c)–(e)

The normal fitness curve for Nc=1 and $\beta = 1$ reaches its maximum after 12 independent trials, remaining within the range, as shown in Figure 8(c). This implies that the algorithm attains stability and optimal performance following a specific threshold of executions. The normal curve depicted in Figure 8(d) for Nc=2 and $\beta = 1$ is bounded by, and after 12 independent trials, it displays a comparable peak. The normal curve illustrated in Figure 8(e) is characterized by a flattened shape within the range, suggesting enhanced stability in comparison to the curves illustrated in Figures 8 (c) and (d) for Nc=3 and BETA=1. The observed flattening implies that as Nc increases, performance becomes more consistent and optimal outcomes ensue.

• Nc=1, 2 and 3 and $\beta = 0.9$ Figure 9 (c)–(e)

The fitness curve for fractional order Beta = 0.9 and Nc = 1 is depicted in Figure 9(c), where it varies from and reaches its maximum after 12 independent trials. The curve remains between for Nc=2 after eight independent trials, shown in Figure 9(d). In contrast, the range is for Nc = 3 and $\beta = 0.9$, and the curve reaches its maximum after 12 independent iterations as in Figure 9(e). The aforementioned observations underscore the influence of Nc on the fitness curve and the consequent

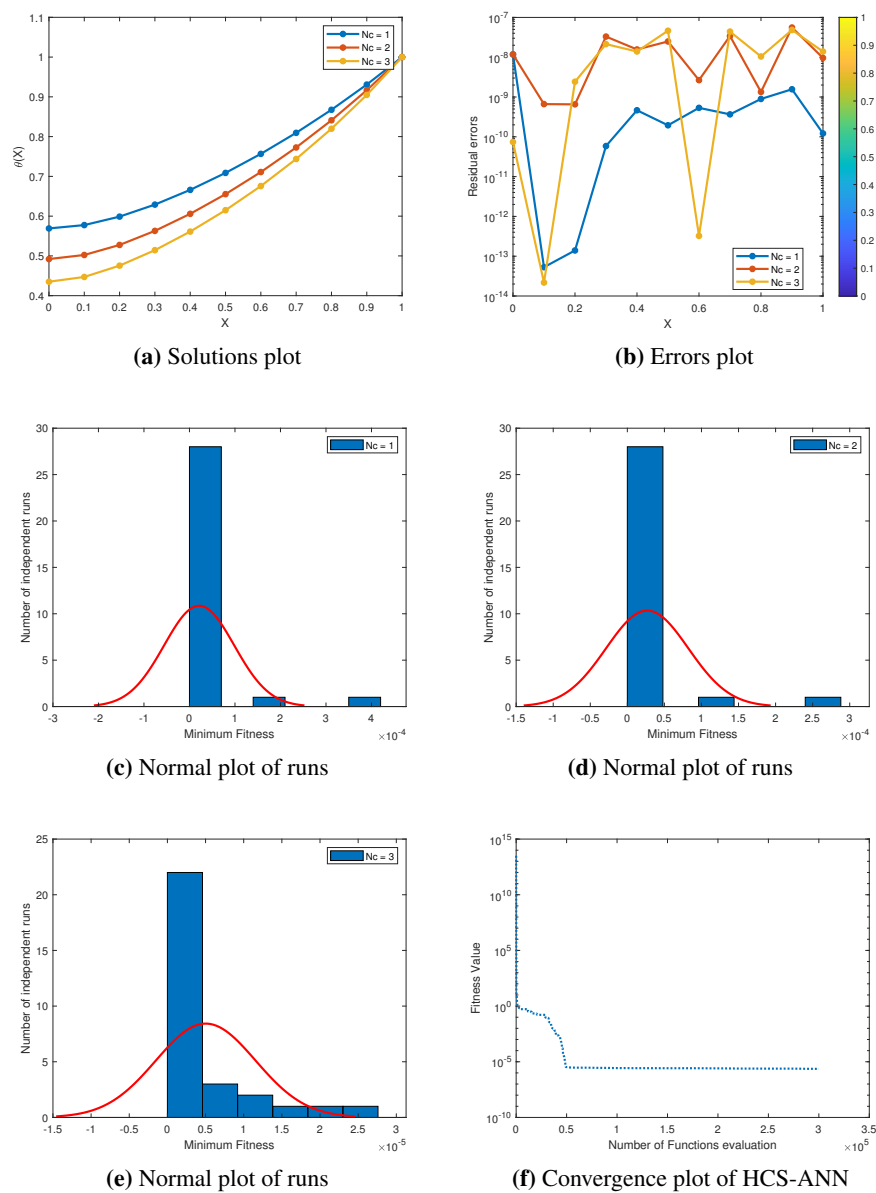convergence characteristics when applied to various fractional orders.

(a) Solutions plot

(b) Errors plot

(c) Normal plot of runs

(d) Normal plot of runs

(e) Normal plot of runs

(f) Convergence plot of HCS-ANN

Figure 11. Graphical results obtained with variation in $Nc = 1, 2, 3$ with fractional-order $\beta = 0.7$.

• Nc = 1, 2 and 3 and $\beta = 0.8$ Figure 10 (c)–(e)

As shown in Figure 10(c), the normal fitness curve for Nc = 1 and $\beta = 0.8$ reaches its optimum after 12 independent trials, remaining within the range. This suggests that the algorithm achieves optimal performance and stability after a predetermined number of executions. The normal curve illustrated in Figure 10(d) for Nc = 2 and $\beta = 0.8$ is delimited by, and it exhibits a similar peak after 8 independent trials and te curve is more flattered than that for Nc = 1. The normal curve depicted in Figure 10(e) exhibits a more uniform shape throughout the range, reached to its peak after 12 trials,

indicating improved stability when compared to the curves for Nc = 3 and β = 0.8 shown in Figure 10 (c) and (d). The flattening observed suggests that as Nc increases, there is a corresponding increase in performance consistency, leading to optimal outcomes.

• Nc = 1, 2 and 3 and β = 0.7 Figure 11 (c)–(e)

Significant insights into the algorithm's performance are uncovered by the normal fitness curves produced by HCS-ANN for 30 independent trials, taking into account various values of the convective-conductive parameter (Nc) and a fractional order β of 0.7. The subsequent enhanced analysis offers a more comprehensive and logical depiction:

The optimal point of the normal fitness curve, which corresponds to Nc = 1 and fractional order β = 0.7, is reached after 12 independent trials and remains consistently within the range, as depicted in Figure 11(c). After a predetermined number of iterations, this behavior indicates that the algorithm converges to an optimal solution, attaining stability and optimum performance.

In Figure 11(d), the normal fitness curve is circumscribed by for Nc = 2 and β = 0.7. It exhibits a comparable peak that transpires marginally earlier, subsequent to ten independent trials. It is worth noting that the curve displays a more angular form in comparison to the one at Nc = 1. The observed flattening implies a potential increase in stability and a more consistent performance, which are both suggestive of enhanced convergence characteristics for the specific combination of parameters in question.

The performance is further illustrated in Figure 11(e) when Nc = 3 and β = 0.7. The curve exhibits a uniform shape throughout the entire range and attains its maximum value after eight trials. The observed flattening in comparison to Figure 11 (c) and (d) indicates that performance consistency improves proportionally with the convective-conductive parameter (Nc). This implies that as Nc increases, outcomes become more stable and dependable, ultimately resulting in the attainment of an optimal solution.

To summarize, the performance of HCS-ANN is significantly impacted by the interaction between the fractional order β and the convective-conductive parameter (Nc), as illustrated by the trends in Figures 11 (c)–(e). The observed increase in curve flattening with Nc indicates enhanced stability and convergence characteristics of the algorithm. This observation offers significant insights into the behavior of the algorithm across various parameter configurations.

• Figure 8–11 (f) convergence plots.

The fitness graphs of the HCS-ANN Deep Learning Algorithm Figures 8–11 (f) offer significant insights regarding its convergence and optimization characteristics. The graphs illustrate effective convergence, as the average fitness value attains stability in the vicinity of function evaluations. The convergence of individual particles is observable through the aggregation of blue lines encircling the red line, thereby augmenting the consistency and reliability of the algorithm. Rapid convergence to optimal solutions is evidenced by the algorithm's overall trend, which demonstrates its efficacy in resolving complex optimization problems. The mean fitness value of the population stabilizes around function evaluations at approximately for Fractional order β = 1, for β = 0.9, for β = 0.8, and for β = 0.7 all are same, around function evaluations shown in Figures 8–11 (f) respectively. In order to comprehend the convergence behavior of the optimization algorithm, it is vital to conduct an analysis of the population's mean fitness value, specifically with regard to various fractional orders β. The stabilization of the mean fitness value for different fractional orders around a specific number of function evaluations is depicted in Figures 8–11(f).

The mean fitness value stabilizes in Figures 8–11(f) around function evaluations of approximately when [β =1]. This implies that when the fractional order is set to 1, the optimization algorithm converges to a stable solution across a consistent range of function evaluations. The reliability of the algorithm in locating the optimal solution is indicated by the stability of the mean fitness value.

In a similar fashion, the mean fitness value stabilizes at around approximately function evaluations when [β = 0.9], the same is for, as illustrated in Figures 9–11 (f) respectively. This further validates the algorithm's capacity to converge consistently over a specified range of function evaluations, notwithstanding a marginally diminished fractional order. Finally, these Figures 8–11 (f) illustrate that the average fitness value remains constant at approximately function evaluations when. This demonstrates the algorithm's ability to converge despite the utilization of a lesser fractional order. The non-dimensional plots are provided in Figure 12 (a) and (b) which shows the decay with time.
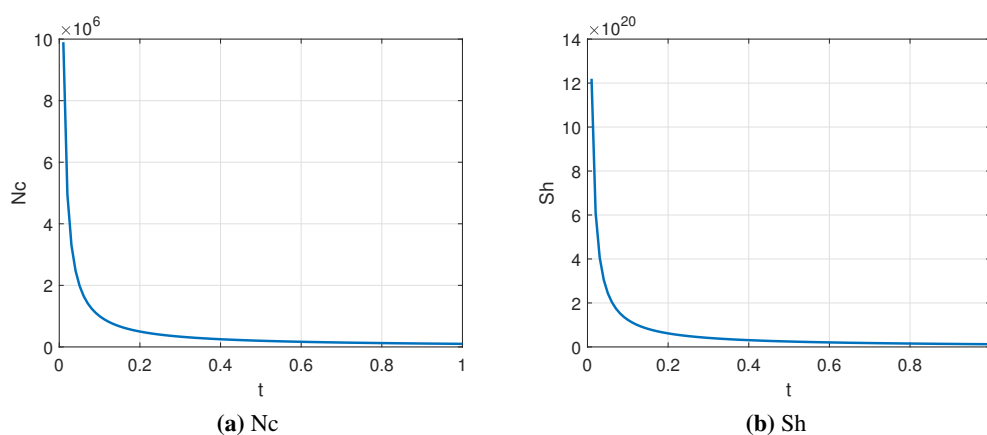

(a) Nc   (b) Sh

Figure 12. Non-dimensional plots for Nc and Sh parameters.

7. Conclusions

The efficacy and resilience of the Hybrid Cuckoo Search Algorithm-based Artificial Neural Network (HCS-ANN) in tackling complex optimization problems are demonstrated through its implementation. A rapid convergence to optimal solutions is observed, providing further evidence of the algorithm's ability to effectively resolve intricate optimization problems.

Significant findings derived from solution plots and analysis:

• Several significant conclusions are deduced through the utilization of solution plots, residual errors, normal fitness curves, and convergence plots.

• A clear inverse relationship between temperature and convection–conduction parameter (Nc) is established as the value of Nc rises from 1 to 3, indicating a consistent trend of decreasing temperature.

• An increase in the Hartmann number (M) results in a more pronounced heat transfer rate across a range of magnetic field angles, which is especially significant in applications such as nuclear reactor fabrication.

The importance of the magnetic field and HCS-ANN in heat transfer:

• The implementation of the Novel HCS-ANN algorithm manipulates the magnetic field to inhibit convection heat transport, thereby improving the average heat transfer through the fin.

• A higher Hartmann number is associated with lower thermal profiles, underscoring the algorithm's versatility in handling diverse scenarios.

1) Evaluation of residual errors and fitness curves:

• Residual errors for both M and Nc are contained within a specified range of, thereby offering a quantitative assessment of the model's accuracy.

• After 30 independent trials, the algorithm's consistent performance is demonstrated by normal fitness curves, which validate its dependability in optimization tasks.

2) The influence of the magnetic field and thermal optimization:

• A marginal reduction in temperature is detected when the magnetic field is inclined, signifying optimized heat transfer.

• The buoyancy force generated by the magnetic field enables improved heat dissipation and heightened heat exchange emanating from the fin.

3) Prospects for future research:

This study lays the groundwork for further investigations into the thermal distribution within radially porous fins when subjected to magnetic effects while damp, an area of particular significance in compact heat exchangers. Additionally, it is advisable to conduct additional research on the intricate physical mechanisms at play by examining the complex interactions among Nc, fractional order beta (BETA), and temperature. In summary, this study provides significant contributions to the understanding of the thermal characteristics of porous radial fins when subjected to an inclined magnetic field. Furthermore, we demonstrate how the HCS-ANN algorithm effectively optimizes the transmission of heat. The observations and correlations that have been identified facilitate progress in the design of heat exchangers and other engineering applications of a similar nature.

Use of AI tools declaration

The authors declare they have not used artificial intelligence (AI) tools in the creation of this article.

Acknowledgments

Conflict of interest

The authors declare no conflicts of interest.

References

1. M. S. Arif, M. Jhangir, Y. Nawaz, I. Abbas, K. Abodayeh, A. Ejaz, Numerical study for magnetohydrodynamic (MHD) unsteady Maxwell nanofluid flow impinging on heated stretching sheet, *Comp. Model. Eng. Sci.*, **133** (2022), 303–325. https://doi.org/10.32604/cmes.2022.020979

2. A. Ejaz, Y. Nawaz, M. S. Arif, D. S. Mashat, K. Abodayeh, Stability analysis of predator-prey system with consuming resource and disease in predator species, *Comp. Model. Eng. Sci.*, **132** (2022), 489–506. https://doi.org/10.32604/cmes.2022.019440

3. R. S. V. Kumar, G. Sowmya, R. Kumar, Execution of probabilists' Hermite collocation method and regression approach for analyzing the thermal distribution in a porous radial fin with the effect of an inclined magnetic field, *Eur. Phys. J. Plus*, **138** (2023), 422. https://doi.org/10.1140/epjp/s13360-023-03986-3

4. U. Khan, R. N. Kumar, A. Zaib, B. C. Prasannakumara, A. Ishak, A. M. Galal, et al., Time-dependent flow of water-based ternary hybrid nanoparticles over a radially contracting/expanding and rotating permeable stretching sphere, *Therm. Sci. Eng. Prog.*, **36** (2022), 101521. https://doi.org/10.1016/j.tsep.2022.101521

5. S. Singh, D. Kumar, K. N. Rai, Analytical solution of Fourier and non-Fourier heat transfer in longitudinal fin with internal heat generation and periodic boundary condition, *Int. J. Therm. Sci.*, **125** (2018), 166–175. https://doi.org/10.1016/j.ijthermalsci.2017.11.029

6. M. Turkyilmazoglu, Heat transfer from moving exponential fins exposed to heat generation, *Int. J. Heat Mass Tran.*, **116** (2018), 346–351. https://doi.org/10.1016/j.ijheatmasstransfer.2017.08.091

7. M. Alkasassbeh, Z. Omar, F. Mebarek-Oudina, J. Raza, A. Chamkha, Heat transfer study of convective fin with temperature-dependent internal heat generation by hybrid block method, *Heat Transf.-Asian Res.*, **48** (2019), 1225–1244. https://doi.org/10.1002/htj.21428

8. M. Kezzar, I. Tabet, M. R. Eid, A new analytical solution of longitudinal fin with variable heat generation and thermal conductivity using DRA, *Eur. Phys. J. Plus*, **135**, (2020), 120. https://doi.org/10.1140/epjp/s13360-020-00206-0

9. S. Y. Kim, J. W. Paek, B. H. Kang, Flow and heat transfer correlations for porous fin in a plate-fin heat exchanger, *J. Heat Transfer.*, **122** (2000), 572–578. https://doi.org/10.1115/1.1287170

10. M. Fathi, M. M. Heyhat, M. Z. Targhi, S. Bigham, Porous-fin microchannel heat sinks for future micro-electronics cooling, *Int. J. Heat Mass Tran.*, **202** (2023), 123662. https://doi.org/10.1016/j.ijheatmasstransfer.2022.123662

11. G. Sowmya, R. S. V. Kumar, Assessment of transient thermal distribution in a moving porous plate with temperature-dependent internal heat generation using Levenberg–Marquardt backpropagation neural network, *Waves Random Complex*, 2023, 1–21. https://doi.org/10.1080/17455030.2023.2198040

12. B. J. Gireesha, G. Sowmya, Heat transfer analysis of an inclined porous fin using differential transform method, *Int. J. Ambient Energy*, **43** (2022), 3189–3195. https://doi.org/10.1080/01430750.2020.1818619

13. J. Wang, Y. P. Xu, R. Qahiti, M. Jafaryar, M. A. Alazwari, N. H. Abu-Hamdeh, et al., Simulation of hybrid nanofluid flow within a microchannel heat sink considering porous media analyzing CPU stability, *J. Petrol. Sci. Eng.*, **208** (2022), 109734. https://doi.org/10.1016/j.petrol.2021.109734

14. V. Venkitesh, A. Mallick, Thermal analysis of a convective–conductive–radiative annular porous fin with variable thermal parameters and internal heat generation, *J. Therm. Anal. Calorim.*, **147** (2022), 1519–1533. https://doi.org/10.1007/s10973-020-10384-9

15. Z. U. Din, A. Ali, M. De la Sen, G. Zaman, Entropy generation from convective–radiative moving exponential porous fins with variable thermal conductivity and internal heat generations, *Sci. Rep.*, **12** (2022), 1791. https://doi.org/10.1038/s41598-022-05507-1

16. R. S. V. Kumar, G. Sowmya, M. C. Jayaprakash, B. C. Prasannakumara, M. I. Khan, K. Guedri, et al., Assessment of thermal distribution through an inclined radiative-convective porous fin of concave profile using generalized residual power series method (GRPSM), *Sci. Rep.*, **12** (2022), 13275. https://doi.org/10.1038/s41598-022-15396-z

17. T. Cyriac, B. N. Hanumagowda, M. Umeshaiah, V. Kumar, J. S. Chohan, R. N. Kumar, et al., Performance of rough secant slider bearing lubricated with couple stress fluid in the presence of magnetic field, *Mod. Phys. Lett. B*, 2023, 2450140. https://doi.org/10.1142/S0217984924501409

18. G. Sharma, B. N. Hanumagowda, S. V. K. Varma, R. N. Kumar, A. S. Alqahtani, M. Y. Malik, Impact of magnetic field and nonlinear radiation on the flow of Brinkmann-type chemically reactive hybrid nanofluid: A numerical study, *J. Therm. Anal. Calorim.*, **149** (2024), 745–759. https://doi.org/10.1007/s10973-023-12720-1

19. P. Srilatha, R. S. V. Kumar, R. N. Kumar, R. J. P. Gowda, A. Abdulrahman, B. C. Prasannakumara, Impact of solid-fluid interfacial layer and nanoparticle diameter on Maxwell nanofluid flow subjected to variable thermal conductivity and uniform magnetic field, *Heliyon*, **9** (2023), e21189. https://doi.org/10.1016/j.heliyon.2023.e21189

20. F. Selimefendigil, H. F. Oztop, A. J. Chamkha, Natural convection in a CuO–water nanofluid filled cavity under the effect of an inclined magnetic field and phase change material (PCM) attached to its vertical wall, *J. Therm. Anal. Calorim.*, **135** (2019), 1577–1594. https://doi.org/10.1007/s10973-018-7714-9

21. R. S. V. Kumar, I. E. Sarris, G. Sowmya, J. K. Madhukesh, B. C. Prasannakumara, Effect of electromagnetic field on the thermal performance of longitudinal trapezoidal porous fin using DTM–Pade approximant, *Heat Transf.*, **51** (2022), 3313–3333. https://doi.org/10.1002/htj.22450

22. Y. J. Wei, A. Rabinovich, The inverse problem of permeability identification for multiphase flow in porous media, *Phys. Fluids*, **35** (2023), 073327. https://doi.org/10.1063/5.0153939

23. B. Jadamba, A. A. Khan, M. Sama, H. J. Starkloff, C. Tammer, A convex optimization framework for the inverse problem of identifying a random parameter in a stochastic partial differential equation, *SIAM/ASA J. Uncertain.*, **9** (2021), 922–952. https://doi.org/10.1137/20M132395

24. T. Liu, Parameter estimation with the multigrid-homotopy method for a nonlinear diffusion equation, *J. Comput. Appl. Math.*, **413** (2022), 114393. https://doi.org/10.1016/j.cam.2022.114393

25. B. Li, T. Zhang, C. Zhang, Investigation of financial bubble mathematical model under fractal-fractional Caputo derivative, *Fractals*, **31** (2023), 2350050. https://doi.org/10.1142/S0218348X23500500

26. M. Caputo, M. Fabrizio, A new definition of fractional derivative without singular kernel, *Progr. Fract. Differ. Appl.*, **1** (2015), 73–85. http://doi.org/10.12785/pfda/010201

27. X. Jiang, J. Li, B. Li, W. Yin, L. Sun, X. Chen, Bifurcation, chaos, and circuit realisation of a new four-dimensional memristor system, *Int. J. Nonlin. Sci. Numer. Simul.*, **24** (2023), 2639–2648. https://doi.org/10.1515/ijnsns-2021-0393

28. D. Baleanu, B. Agheli, M. M. Al Qurashi, Fractional advection differential equation within Caputo and Caputo–Fabrizio derivatives, *Adv. Mech. Eng.*, 2016. https://doi.org/10.1177/1687814016683305

29. I. A. Mirza, D. Vieru, Fundamental solutions to advection–diffusion equation with time-fractional Caputo–Fabrizio derivative, *Comput. Math. Appl.*, **73** (2017), 1–10. https://doi.org/10.1016/j.camwa.2016.09.026

30. H. Sun, X. Hao, Y. Zhang, D. Baleanu, Relaxation and diffusion models with non-singular kernels, *Physica A Stat. Mech. Appl.*, **468** (2017), 590–596. https://doi.org/10.1016/j.physa.2016.10.066

31. A. Atangana, D. Baleanu, New fractional derivatives with non-local and non-singular Kernel, theory and application to heat transfer model, *Therm. Sci.*, **20** (2016), 763–769. https://doi.org/10.2298/TSCI160111018A

32. X. Zhu, P. Xia, Q. He, Z. Ni, L. Ni, Coke price prediction approach based on dense GRU and opposition-based learning salp swarm algorithm, *Int. J. Bio-Inspir. Comput.*, **21** (2023), 106–121. https://doi.org/10.1504/IJBIC.2023.130549

33. X. Zhu, P. Xia, Q. He, Z. Ni, L. Ni, Ensemble classifier design based on perturbation binary salp swarm algorithm for classification, *CMES-Comp. Model. Eng. Sci.*, **135** (2023), 653–671. https://doi.org/10.32604/cmes.2022.022985

34. C. Kumar, P. Nimmy, K. V. Nagaraja, R. S. V. Kumar, A. Verma, S. Alkarni, et al., Analysis of heat transfer behavior of porous wavy fin with radiation and convection by using a machine learning technique, *Symmetry*, **15** (2023), 1601. https://doi.org/10.3390/sym15081601

35. S. Jayan, K. V. Nagaraja, A general and effective numerical integration method to evaluate triple integrals using generalized Gaussian quadrature, *Procedia Eng.*, **127** (2015), 1041–1047. https://doi.org/10.1016/j.proeng.2015.11.457

36. S. B. Prakash, K. Chandan, K. Karthik, S. Devanathan, R. S. V. Kumar, K. V. Nagaraja, et al., Investigation of the thermal analysis of a wavy fin with radiation impact: an application of extreme learning machine, *Phys. Scr.*, **99** (2023), 015225. https://doi.org/10.1088/1402-4896/ad131f

37. O. J. J. Algahtani, Comparing the Atangana–Baleanu and Caputo–Fabrizio derivative with fractional order: Allen Cahn model, *Chaos Soliton. Fract.*, **89** (2016), 552–559. https://doi.org/10.1016/j.chaos.2016.03.026

38. R. S. V. Kumar, M. D. Alsulami, I. E. Sarris, B. C. Prasannakumara, S. Rana, Backpropagated neural network modeling for the non-fourier thermal analysis of a moving plate, *Mathematics*, **11** (2023), 438. https://doi.org/10.3390/math11020438

39. S. M. Hussain, R. Mahat, N. M. Katbar, I. Ullah, R. S. V. Kumar, B. C. Prasannakumara, et al., Artificial neural network modeling of mixed convection viscoelastic hybrid nanofluid across a circular cylinder with radiation effect: Case study, *Case Stud. Therm. Eng.*, **50** (2023), 103487. https://doi.org/10.1016/j.csite.2023.103487

40. W. Waseem, M. Sulaiman, S. Islam, P. Kumam, R. Nawaz, M. A. Z. Raja, et al., A study of changes in temperature profile of porous fin model using cuckoo search algorithm, *Alex. Eng. J.*, **59** (2020), 11–24. https://doi.org/10.1016/j.aej.2019.12.001

41. I. Podlubny, *Fractional differential equations: An introduction to fractional derivatives, fractional differential equations, to methods of their solution and some of their applications*, Elsevier, 1998.

42. F. Wang, R. S. V. Kumar, G. Sowmya, E. R. El-Zahar, B. C. Prasannakumara, M. I. Khan, et al., LSM and DTM-Pade approximation for the combined impacts of convective and radiative

heat transfer on an inclined porous longitudinal fin, *Case Stud. Therm. Eng.*, **35** (2022), 101846. https://doi.org/10.1016/j.csite.2022.101846

43. K. R. Madhura, B. G. Kalpana, O. D. Makinde, Thermal performance of straight porous fin with variable thermal conductivity under magnetic field and radiation effects, *Heat Transf.*, **49** (2020) 5002–5019. https://doi.org/10.1002/htj.21864

44. P. L. Ndlovu, R. J. Moitsheki, Analysis of temperature distribution in radial moving fins with temperature dependent thermal conductivity and heat transfer coefficient, *Int. J. Therm. Sci.*, **145** (2019), 106015. https://doi.org/10.1016/j.ijthermalsci.2019.106015